

## Highly non-linear interlayer exciton-polaritons in bilayer MoS<sub>2</sub>

Biswajit Datta,<sup>1</sup> Mandeep Khatoniar,<sup>1,2</sup> Prathmesh Deshmukh,<sup>1,2</sup> Rezlind Bushati,<sup>1,2</sup>  
Simone De Liberato,<sup>3</sup> Stephane Kena Cohen,<sup>4</sup> and Vinod M. Menon<sup>1,2, a)</sup>

<sup>1)</sup>*Department of Physics, City College of New York, New York, NY,  
USA*

<sup>2)</sup>*Department of Physics, Graduate Center of the City University of New York  
(CUNY), New York, NY, USA*

<sup>3)</sup>*School of Physics and Astronomy, University of Southampton, Southampton,  
UK*

<sup>4)</sup>*Department of Engineering Physics, École Polytechnique de Montréal, Montréal,  
Quebec, Canada*

Realizing nonlinear optical response in the low photon density limit in solid state systems has been a long-standing challenge. Semiconductor microcavities in the strong coupling regime hosting light-matter quasi-particles called exciton-polaritons have emerged as an attractive candidate in this context. However, the weak interaction between these quasi-particles has been a hurdle in this quest. Two-dimensional transition metal dichalcogenides (TMDCs) owing to their inherently large oscillator strength and the wide array of excitonic complexes they host present an opportunity to address this challenge. Among the different excitations supported by TMDCs, a prime candidate is the interlayer excitons that form in heterostructures of TMDCs. Due to the spatial separation of the electron and holes in different layers, they have a permanent dipole moment making them interact stronger. This advantage is often diminished by their poor oscillator strength making them unsuitable for realizing polaritons. The recent discovery of interlayer excitons in naturally occurring homobilayer MoS<sub>2</sub> alleviates this issue owing to their hybrid characteristics arising from the interlayer charge transfer state and intralayer B exciton. Here we demonstrate the strong coupling of interlayer excitons in bilayer MoS<sub>2</sub> with cavity photons resulting in unprecedented nonlinear interaction strengths. A ten-fold increase in nonlinearity is observed for the interlayer excitons compared to the conventional A excitons which have been used extensively for strong coupling studies. The measured interaction strength in the weak pump limit is  $\sim (100 \pm 2) \mu\text{eV} \mu\text{m}^2$ . The observed nonlinear response is attributed to a combination of both exciton-exciton interaction and saturation due to phase space filling. The formation of the interlayer exciton-polaritons in naturally occurring homobilayers of TMDCs makes them very attractive for scalability. These highly nonlinear interlayer exciton-polaritons are likely to be a frontrunner in the quest for solid-state quantum nonlinear devices.

---

<sup>a)</sup>vmenon@ccny.cuny.edu

Photons are becoming ubiquitous in emerging quantum technologies like quantum communication and metrology due to the ability to propagate long distances while being robust against decoherence<sup>1,2</sup>. To further extend the span of their utilities, platforms to achieve and implement strongly interacting photons in solid-state systems are much-sought after<sup>3</sup>. Conventional materials do not exhibit nonlinear response at power levels associated with single photons. In this context, remarkable advances have been made in cold atom systems to realize interacting photons at the single-particle level<sup>4</sup>. A strong contender for the generation of strongly interacting photons in the solid-state are exciton-polaritons formed via non-perturbative coupling of cavity photons with excitonic resonances. Although they can be modeled as non-interacting quantum fluids at low densities, beyond a critical density, saturation and short-range exchange interactions become significant and give rise to various phenomena like the appearance of spontaneous coherence, parametric down-conversion, and superfluidity<sup>5</sup>. Strong spatial confinement along with Coulomb interactions give rise to even stronger correlations between polaritons that can no longer be described using a mean-field theory. Such interactions give rise to non-Poissonian statistics of laser transmission, dubbed as polariton blockade. Preliminary evidence of such non-classical correlation was recently observed in confined polariton systems in GaAs<sup>6,7</sup>. The small ratio of interaction to dissipation rates resulted in only a weak violation of classical correlations. Formation of polaritons with excitons that possess a permanent dipole moment has been shown to enhance the polariton interactions both in resonant<sup>8,9</sup> and non-resonant excitation schemes<sup>10</sup>.

Transition metal dichalcogenides (TMDCs) have garnered much attention for their exceptional optoelectronic properties and have been used to demonstrate wide array of fundamental phenomena as well as technological applications<sup>11</sup>. Furthermore, their two-dimensional (2D) nature allows for the formation of heterojunctions or homojunctions with arbitrary twist angles resulting in emergent properties<sup>12-15</sup>. Their strong binding energy along with large oscillator strength, renders them capable of forming polaritons at room temperature<sup>16</sup>, which has also been shown to retain the intriguing properties of the 2D excitons<sup>17-19</sup>. Polariton interactions in TMDCs under different configurations are being studied extensively. Realization of Fermi polarons<sup>20</sup>, trion polaritons<sup>21,22</sup>, and excited-state exciton-polaritons<sup>23</sup> have shown great potential in their abilities to harness strong polariton interactions. Moiré exciton-polaritons were recently demonstrated using heterobilayers of WS<sub>2</sub>/MoSe<sub>2</sub> where

the electronic confinement potential arising from the twisted heterostructure was shown to enhance the nonlinearity<sup>12</sup>. However, all the platforms above rely on short-range exchange interactions that pose a bottleneck in realizing few polariton non-linearity under current experimental capabilities.

In this context, a very attractive possibility is the use of spatially indirect interlayer excitons (IE) in TMDC heterostructures<sup>24</sup> that can have a permanent dipole moment and hence support highly interacting dipolar polaritons. However, their inherently low oscillator strength creates an impediment in reaching the strong coupling regime. Furthermore, the large in-built interfacial electric fields make electrical tuning of the energies of the IE far more difficult. Bilayer MoS<sub>2</sub> provides a highly attractive platform to solve these issues<sup>25-28</sup>. The IE in naturally stacked 2H bilayer MoS<sub>2</sub> remarkably has both an out of plane (static) dipole moment and an in-plane (oscillating) dipole moment. Due to the in-plane dipole moment, the IE in MoS<sub>2</sub> bilayer has an oscillator strength of approximately 36% of that of the intralayer A exciton along with strong absorption that is visible up to room temperatures. Moreover, a strong response to DC electric fields has been demonstrated in these systems, thus confirming their dipolar nature<sup>25,26,28</sup>. In this work, we achieve strong coupling of microcavity photons with the IEs (along with intralayer A and B excitons) in bilayer MoS<sub>2</sub>. The IE polariton shows 10 fold enhancement of the polariton nonlinearity compared to the intralayer A exciton, making it an appealing platform to realize strongly interacting polaritons in condensed matter systems. In addition, the ease of fabrication and realization of multi-polariton species in this system makes it a practical and fundamentally interesting material for studying polariton physics.

Fig. 1a shows schematic of the bands that form interlayer exciton (IE) in bilayer MoS<sub>2</sub>. IE<sub>1</sub> and IE<sub>2</sub> excitons in which electrons are in layer 1 and layer 2 respectively remain degenerate at zero external bias. The hole is always delocalized among both layers. The black arrows connect the bands that form the IE. This peculiar charge distribution is at the heart of producing both in-plane and out-of-plane dipole moments of IE. Fig. 1b shows the charge distribution in real space for IE<sub>1</sub> and IE<sub>2</sub>. Owing to the spatial separation of the electron and the hole, it acquires a permanent dipole moment, the nature of which has been a topic of much interest recently<sup>25-28</sup>. IEs in MoS<sub>2</sub> homobilayer can be thought of as an admixture of B intralayer exciton with an optically dark but electric field tunable charge-transfer exciton, which is typically found in TMDC heterobilayers<sup>29</sup>. As a result, IEs in MoS<sub>2</sub> homobilayer

acquires both a strong oscillator strength and electric field tunability<sup>29</sup>. Fig. 1c shows the white light differential reflection of the bilayer sample at 77 K. The peaks at 1.933 eV, 1.995 eV, and 2.10 eV correspond to the A, IE, and B excitons, respectively. The absorption of the IE is found to be ~36% of the A exciton’s absorption. Interestingly, the absorption of the IE is discernible even at room temperature, which provides a straightforward method to identify the MoS<sub>2</sub> bilayer flakes after mechanical exfoliation.

Fig. 2a shows the schematic of the structure used in this experiment. It consists of a bilayer MoS<sub>2</sub> encapsulated by thin (20 nm) hexagonal boron nitride (hBN), which is sandwiched between a bottom dielectric distributed Bragg reflector (DBR) mirror and a top silver mirror. See Supplementary Note I and Methods for the fabrication details and cavity structure. The cavity is designed such that the bilayer MoS<sub>2</sub> flake sits close to an electric field anti-node, allowing us to observe five dispersive modes associated with the different polaritonic states as shown in Fig. 2b. These distinct polariton modes arise due to the hybridization of the cavity photon mode with the various excitonic states present in the bilayer system. We name the polariton branches as pol-1 through pol-5, with pol-1 corresponding to the lowest energy and pol-5 the highest. Interestingly, besides the 1s states of A, and B excitons, the IE and 2s Rydberg state of A exciton (which lies slightly below the B (1s) exciton) also show strong coupling at 7 K temperature. We fit the data with a five-coupled oscillator model where the energy of all the four excitons, the cavity mode, their Rabi splitting, and the effective refractive index of the system are treated as fit parameters. The fit results in exciton energies  $E_{A1s} = 1.9323$  eV,  $E_{IE} = 2.0014$  eV,  $E_{A2s} = 2.0819$  eV,  $E_{B1s} = 2.0994$  eV and the Rabi splittings  $\Omega_{A1s} = 40.4$  meV,  $\Omega_{IE} = 21.4$  meV,  $\Omega_{A2s} = 26$  meV,  $\Omega_{B1s} = 51$  meV. The exciton energies obtained through the fit agree well with the experimentally determined exciton energies with slight shifts due to the strain and changes in the dielectric environment in the cavity. In our device, the bare cavity mode is  $\delta_{C-A_X} = 20$  meV positively detuned with respect to the A (1s) exciton. See Supplementary Note II for details on the coupled oscillator model. We notice that the Rabi splitting of the IE polariton remains observable even at 77 K but not at room temperature due to increased damping at a higher temperature. On the other hand, 1s state of A and B excitons remain strongly coupled even at room temperature due to their larger oscillator strength. See Supplementary Note III for the data at 77 K.

We measured the white light reflectivity around the IE and A resonance and monitor the

energy shifts of the polariton branches, see Supplementary Note V for the details. Fig. 3a shows the energy of the upper and lower branch of the IE polariton as a function of polariton density at the inplane wavevector corresponding to the zero detuning  $k_{\parallel}$  (where the cavity mode and exciton energy are degenerate). We fit Lorentzians at each density to obtain the energy of the upper and lower polaritons. See Supplementary Note IV for details of the polariton density calculation and Supplementary Note V for the raw data of the density dependent differential reflection data of IE polariton. We can see from Fig. 3a that the lower branch of the IE polariton moves with power more than the upper branch at the zero-detuning  $k_{\parallel}$ . We also observe a simultaneous increase of the zero-detuning  $k_{\parallel}$  and the decrease of Rabi splitting (at the zero-detuning  $k_{\parallel}$ ) with increasing density. This suggests the presence of both exciton energy renormalization and saturation effect. See Supplementary Note VIII for the density dependent Rabi splitting of IE polariton. Taking the derivative of the  $E_{LP}$  with respect to density, we calculate the strength of the nonlinearity,  $g_{LP}$ . Since the rate of blue shift saturates at high density (olive color curve in Fig. 3a),  $g_{LP}^{IE}$  reduces with polariton density as seen in Fig. 3b. Note that at the lowest powers accessible in our measurement, the IE LP already shows a power-dependent blueshift. On the other hand, within the accessible range of the polariton density in our experiment,  $g_{LP}^A$  remains nearly a constant (see Supplementary Note IX and Supplementary Fig.S8 for the blueshift data of the lower branch of A polariton). The obtained strength of the non-linearity in the low density limit for IE and A polaritons are  $g_{LP}^{IE} \sim (100 \pm 2) \text{ } \mu\text{eV } \mu\text{m}^2$  and  $g_{LP}^A \sim (10 \pm 0.2) \text{ } \mu\text{eV } \mu\text{m}^2$  respectively. For IE polariton, we find a significant  $\sim 10$  fold increase in the nonlinearity compared to the A exciton-polariton. This  $g_{LP}^A$  value for pol-1 is comparable to the previous report for A exciton-polariton in monolayer WSe<sub>2</sub><sup>23</sup>.

We now proceed to discern the contributions from nonlinearities arising from renormalization of the exciton energy ( $\Delta E_{\text{exc-exc}}$ ) and reduction of the oscillator strength of the exciton due to phase space filling ( $\Delta E_{\text{sat}}$ ) to the energy shift of pol-2 and pol-3. Fig. 4a shows the Hopfield coefficients of all the excitons and the cavity as a function of  $k_{\parallel}$  which is later used to plot  $\Delta E_{LP}^{IE}$  as a function of Hopfield cavity fraction ( $C$ ). The Hopfield coefficients of A exciton-polariton is given in Supplementary Note VII. We measure the energy shift  $\Delta E_{LP}^{IE}$  (of pol-2) as a function of the Hopfield cavity fraction, see Fig. 4b. The interaction strength due to phase space filling in a single excitonic system can be written in terms of  $g_{LP} = 4g_{\text{SAT}}|C||X|^3$ , where X is the Hopfield coefficient for the exciton. Although this is

a multi exciton system, the contribution of the other excitons close to the zero detuning  $k_{\parallel}$  of the IE is small. Neglecting other excitons we can write  $g_{\text{LP}}^{\text{IE}} = 4g_{\text{SAT}}|C|(1 - |C|^2)^{3/2}$  which is a non-monotonic function of the cavity Hopfield coefficient as shown in the Fig. 4b inset (red curve). Similarly, considering only exciton-exciton interaction, the energy scales as  $g_{\text{LP}} = g_{\text{XX}}|X|^4 = g_{\text{XX}}(1 - |C|^2)^2$  which monotonically decreases with increasing  $|C|$  (cyan curve in Fig. 4b inset). We find that the measured nonlinear response of the IE polariton (at the Rabi splitting of pol-2 and pol-3) is the highest at an in-plane wave vector larger than zero detuning  $k_{\parallel}$ , as seen in Fig. 4b. We also notice that  $\Delta E_{\text{LP}}^{\text{IE}}$  changes non-monotonically with the cavity Hopfield coefficient. The qualitative resemblance of the measured  $\Delta E_{\text{LP}}^{\text{IE}}$  with the non-monotonic saturation effect suggests that it is the dominant mechanism dictating the nonlinearity in our system. However, the appearance of the  $\Delta E_{\text{LP}}^{\text{IE}}$  peak at a  $|k_{\parallel}| > \text{zero}$  detuning  $k_{\parallel}$  and increase of zero detuning  $k_{\parallel}$  at higher density points to a sizable contribution of the  $\Delta E_{\text{exc-exc}}$ . Fig. 4c shows a schematic of the polariton energies at two different powers for  $\Delta E_{\text{sat}} > \Delta E_{\text{exc-exc}}$ . Due to both the blue shift of the exciton and saturation effect, the lower branch moves with increasing power more than the upper branch. Analyzing the blueshift of the IE lower polariton branch and redshift of the IE upper polariton branch we calculate the magnitude of  $\Delta E_{\text{exc-exc}}$  and  $\Delta E_{\text{sat}}$  in our system. At the zero detuning  $k_{\parallel}$  we write the energy shift of pol-2 as  $\Delta E_{\text{LP}}^{\text{IE}} = \Delta E_{\text{exc-exc}} + \Delta E_{\text{sat}}$  and the energy shift of pol-3 as  $\Delta E_{\text{UP}}^{\text{IE}} = \Delta E_{\text{exc-exc}} - \Delta E_{\text{sat}}$ . From these equations we obtain  $\Delta E_{\text{exc-exc}}$  and  $\Delta E_{\text{sat}}$  as a function of polariton density, as shown in Fig. 4d. This shows magnitude of  $\Delta E_{\text{sat}}$  in our system is larger than  $\Delta E_{\text{exc-exc}}$  by roughly a factor of 2.

The polaritons interact with each other due to their excitonic part in the wavefunction. In general, the Coulomb interaction of excitons has both direct and exchange contributions. For a regular intralayer exciton (such as A exciton in our system), the direct Coulomb energy goes to zero for small wavevector<sup>30</sup>. Hence for intralayer excitons in TMDC, the exchange term dominates. On the contrary, due to the separation of electrons and holes in two different layers for interlayer excitons in heterobilayer TMDC, the exchange term is negligible. At the same time, the direct term is non-zero even at small wavevectors for interlayer excitons<sup>30</sup>. As a result, the direct Coulomb term is the dominating energy correction for interlayer excitons as shown theoretically in ref.<sup>30</sup>. The direct interaction for small momenta scales with the fourth power of excitonic Bohr radius<sup>30</sup>. Moreover, the saturation density is inversely proportional to its second power and depends on the details of

the excitonic wavefunction<sup>31</sup>. A smaller binding energy has been reported in the literature for IE compared to the A exciton (112 meV and 163 meV respectively<sup>26</sup>), as expected from the increased real-space charge separation in the former. The corresponding larger Bohr radius will thus lead to higher interaction energy and smaller saturation density. This is a plausible reason for our observed 10 fold enhancement in the nonlinearity for the IE compared to the A exciton. The delocalized hole wavefunction of the IE that affects the tunneling of the interlayer carrier in favor of exchange-like interactions could also contribute to the large non-linearity. However, there is no report of the quantitative enhancement of the Bohr radius for IE in bilayer MoS<sub>2</sub>. Due to these factors, it is hard to pin down the exact mechanism for our observed enhancement in the nonlinearity for the interlayer exciton and calls for more theoretical and experimental investigations. But, to corroborate our findings we perform similar power-dependent reflectivity on a bilayer MoS<sub>2</sub> system without the top mirror. The IEs saturate at an order of magnitude lower excitation power than the A excitons, indicating a presence of strong saturation mechanisms. For more details see Supplementary Note VI and Supplementary Figure 5.

In summary, we demonstrate extremely large optical nonlinearity arising from IE polaritons in homobilayer MoS<sub>2</sub>. The reported nonlinearity is an order of magnitude larger than that reported for the A excitons in TMDCs bringing the IE polaritons closer to the polariton blockade regime. The bilayer MoS<sub>2</sub> system presents itself as a highly attractive platform to realize IE polaritons and exploit their nonlinear responses with the potential to reach elevated operational temperatures. Further studies including field-dependent tuning of the IE polaritons are required to shed light on the various channels of interactions possible in this system along with the possibility of realization of true dipolar polaritons in TMDCs.

## METHODS

The DBR used in our experiment is made of 8 pairs of SiO<sub>2</sub> (104.9 nm) and TiO<sub>2</sub> (64.7 nm) layers and were deposited by radio frequency sputtering on an intrinsic Si chip. MoS<sub>2</sub> and hBN were exfoliated from bulk crystals (from 2Dsemiconductor Inc.) using blue tape (Nitto) and scotch tape respectively. MoS<sub>2</sub> was exfoliated onto PDMS substrate and hBN was exfoliated onto a 300 nm SiO<sub>2</sub>/Si substrate. Bilayer MoS<sub>2</sub> flakes were identified by reflection spectroscopy – the additional dip at  $\sim 639$  nm in the reflection signal at room tempera-

ture is the hallmark of bilayer MoS<sub>2</sub>. hBN/bilayer MoS<sub>2</sub>/hBN heterostructure stacking and transfer were done using the well-known polypropylene carbonate transfer technique<sup>32</sup>. The chosen top and bottom hBN layers were of similar thickness  $\sim 20$  nm. The final stack was then transferred onto the DBR at a temperature of 150°C. The chip was kept in chloroform for 12 hours to remove the polypropylene carbonate residue. 240 nm polymethylmethacrylate (PMMA) (495 A4 from Michrochem) was spin-coated to form a  $3\lambda/2$  cavity. Finally, a silver layer (40 nm) was deposited by electron-beam evaporation for the top mirror of the microcavity. Optical images of the device and the bare cavity response are given in Supplementary Note I.

We recorded the angle-resolved reflection spectra using Fourier space imaging technique. A broadband halogen light source was used for reflection measurements. A supercontinuum pulsed light source (NKT Photonics, repetition rate 80 MHz, pulse duration 20 ps) was used to study the power dependence of the bare excitons and polaritons. Appropriate long pass and short pass filters were used in the input to excite a narrow band around the excitons/polaritons under study. For the IE polariton, the excitation bandwidth of the supercontinuum laser was chosen to be  $\sim 40$  meV around the IE energy in the power-dependent measurements. The set-up was coupled with a Princeton Instruments monochromator with a CCD camera. A 50X, 0.65 numerical aperture objective was used for all the measurements at 7 K in a closed cycle Montana cryostat. The polariton dispersion was revealed by imaging the back aperture of the microscope objective (Fourier plane) onto the camera. The spot size of the laser was  $1 \mu\text{m}^2$  on a uniform area of the sample of dimension  $\sim 500 \mu\text{m}^2$ .

## ACKNOWLEDGEMENTS

We acknowledge support from ARO MURI program (W911NF-17-1-0312); NSF DMR-2011738, and NSF OMA 1936351. The low temperature spectroscopy facility was supported by NSF MRI grant - DMR-1726573. S.D.L. acknowledges support from a Royal Society Research Fellowship and from the Philip Leverhulme Prize of the Leverhulme Trust.

## CONTRIBUTIONS

V.M.M., M.K. and B.D. conceived the experiments. B.D. fabricated the device. R.B. helped in the fabrication. B.D., M.K. and P.D. performed the measurements. B.D. led the data analysis with inputs from M.K., P.D. and V.M.M. S.D.L. and S.K.C. gave inputs in the data interpretation. B.D, M.K. and V.M.M wrote the manuscript with comments from all authors.

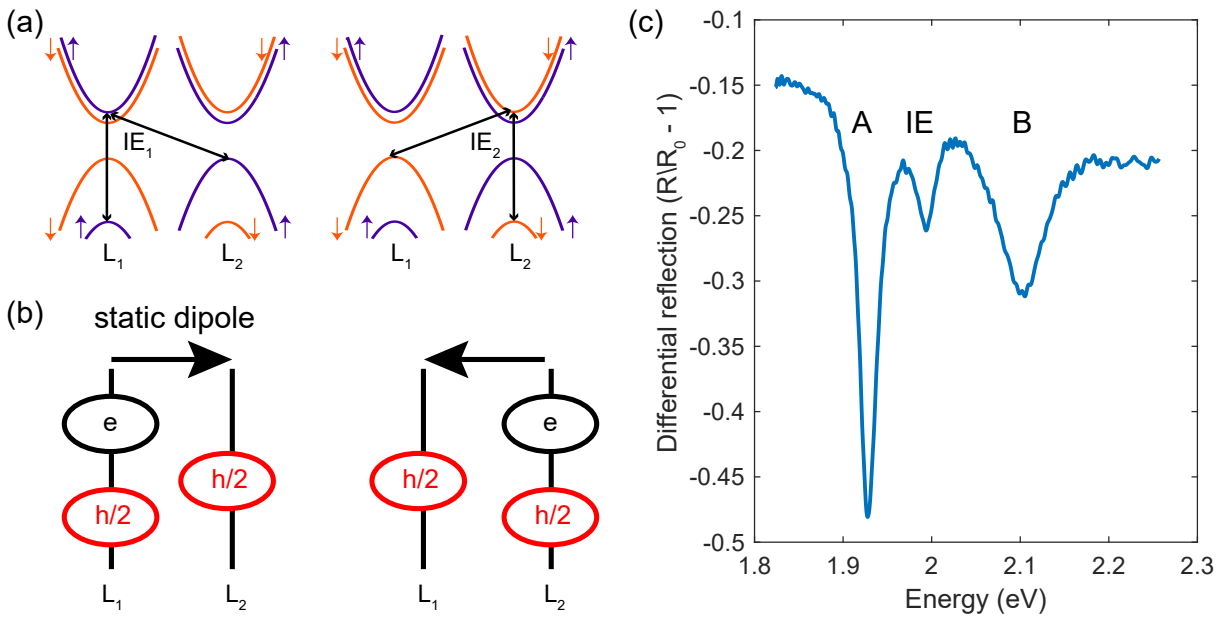
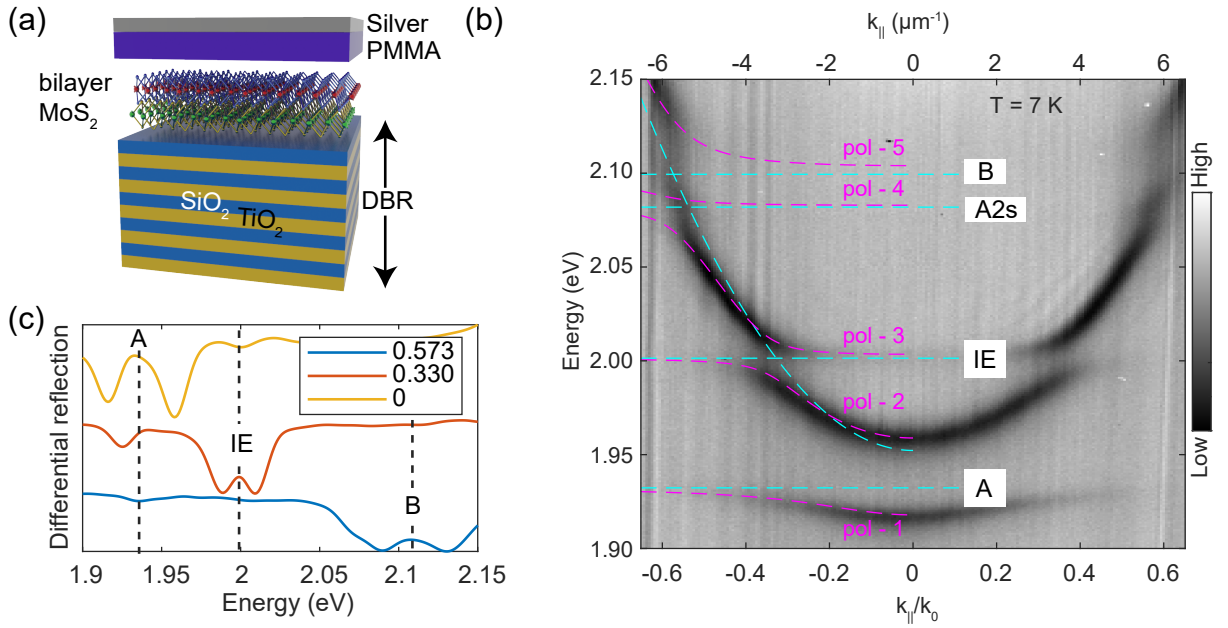


FIG. 1. **Excitons in MoS<sub>2</sub> bilayer and white light absorption.** (a) Schematic of the band structure (around the K point) of the bilayer MoS<sub>2</sub> showing (black arrows) the participation of the different bands in the IE formation. The blue and red colors represent the up and down spin, respectively. L<sub>1</sub> and L<sub>2</sub> refer to the layer 1 and layer 2 of the bilayer MoS<sub>2</sub>, respectively. (b) Schematic showing the two possible charge configurations in the absence of bias voltage between the two layers. In both cases, electron is localized in one of the layers and the hole is distributed among both the layers. (c) White-light absorption at 77 K showing three dips corresponding to A, IE, and B exciton, respectively.



**FIG. 2. Device schematic and polariton dispersion.** (a) Schematic of the device. The bilayer MoS<sub>2</sub> is sandwiched between two hexagonal boron nitride flakes of almost similar thickness  $\sim 20$  nm. The entire stack is transferred by the PPC method onto a SiO<sub>2</sub> terminated SiO<sub>2</sub>-TiO<sub>2</sub> DBR. As the cavity spacer, a layer of 240 nm thick PMMA was spin-coated on the stack. Finally, 40 nm of Ag was e-beam deposited to form a  $3\lambda/2$  cavity, where  $\lambda$  is the wavelength of the cavity resonance. (b) White light differential reflection showing all branches of the polaritons at 7 K. 1s and 2s states of A exciton, IE, and B exciton all are strongly coupled to the same cavity mode. The purple dashed lines are the polariton eigenvalues obtained from fit using four coupled oscillator model. The cyan dashed lines denote the location of the excitons resulting from the fitting:  $E_{A1s} = 1.9323$  eV,  $E_{IE} = 2.0014$  eV,  $E_{A2s} = 2.0819$  eV,  $E_{B1s} = 2.0994$  eV. And  $k_0 = \frac{2\pi}{\lambda_c}$ ;  $\lambda_c$  is the wavelength of the cavity dispersion at  $k_{\parallel} = 0$ . (c) Line cuts at different  $k_{\parallel}$  of the color plot shown in panel-b. It clearly shows that each exciton strongly couples and result in two polariton modes that lie above and below the excitonic resonances.

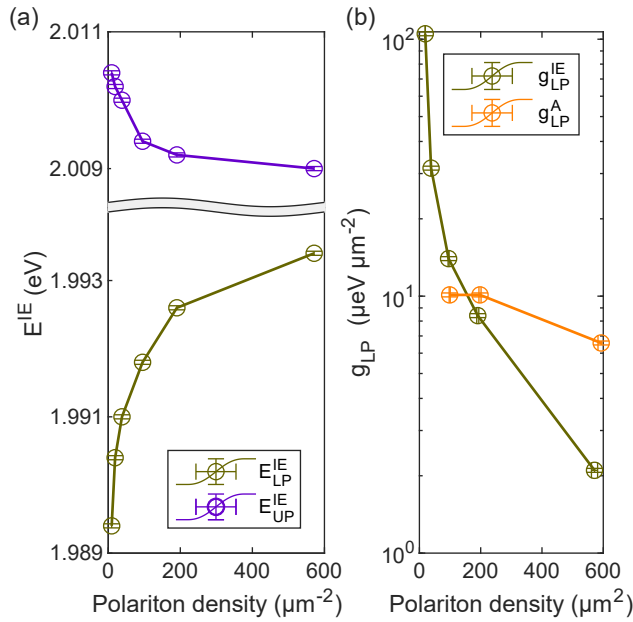


FIG. 3. **Comparison of nonlinearity of the IE polariton with A exciton polariton.**

(a) Energy of the lower and upper branch of the IE polariton as a function of density at zero detuning  $k_{\parallel}$ . We notice that the movement of the lower branch is more than the upper branch – this is due to the combined effect of exciton-exciton interaction and saturation. The error bars in energy represent the uncertainty in determining the peak of the Lorentzian fit (polariton energy) to the reflection data. (b) Strength of the nonlinearity ( $g_{LP}$ ) at zero detuning  $k_{\parallel}$  as a function of the density. We define  $g_{LP}$  as the local slope of the polariton energy vs. density graph shown in previous panel.  $g_{LP}^A$  and  $g_{LP}^{IE}$  are calculated from the pol-1 (lower branch of A polariton) and pol-2 (lower branch of IE polariton) branch, respectively. Note that the  $g_{LP}$  of IE polariton  $\sim (100 \pm 2)$   $\mu\text{eV} \mu\text{m}^2$  is almost 10 times larger than the  $g_{LP}$  of A exciton polariton  $\sim (10 \pm 0.2)$   $\mu\text{eV} \mu\text{m}^2$ . The density error bars take into account the error in measuring power and determining the energy of the polariton and linewidth. The error bars in  $g_{LP}$  take into account the error in determining density and the energy of the polariton.

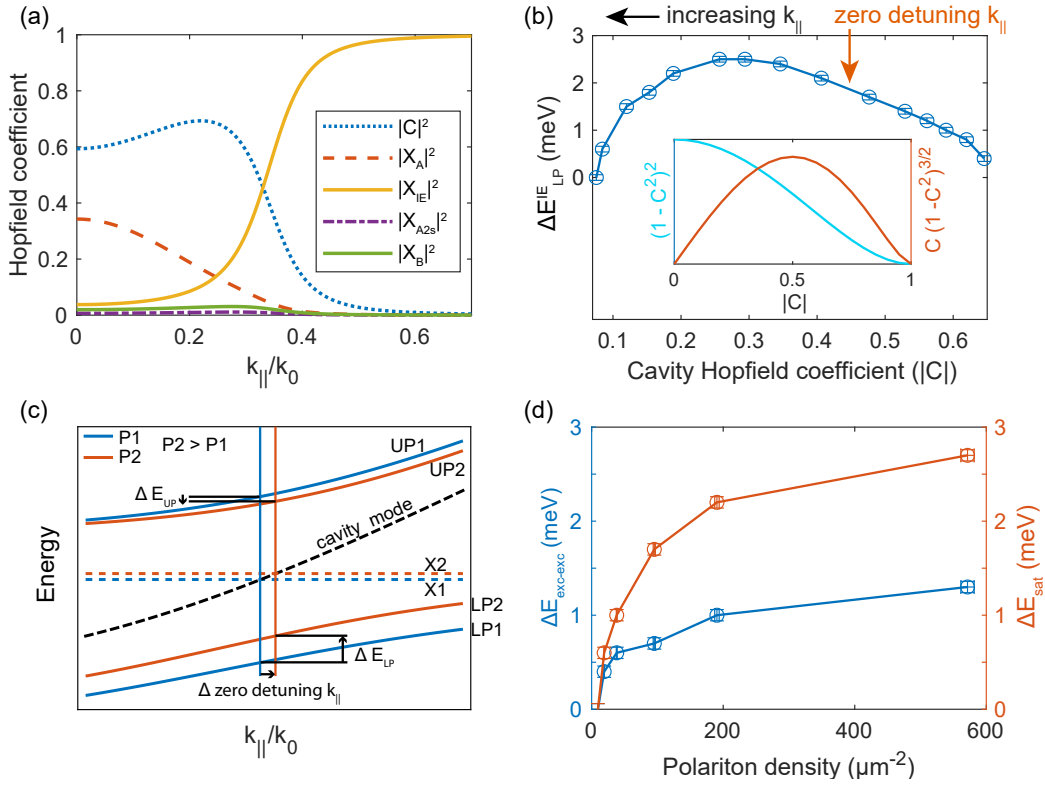


FIG. 4. **Nonlinear response of the IE polariton.** (a) The Hopfield coefficients of the lower IE polariton showing the contributions of cavity photon and the four excitons as a function of  $k_{\parallel}$ . (b) Experimentally measured strength of nonlinearity as a function of cavity Hopfield coefficient. Angle is converted to cavity Hopfield coefficient using the previous plot. We note that the blueshift of the lower branch of IE ( $\Delta E_{LP}^{IE}$ ) is highest close to the zero detuning  $k_{\parallel}$ , but the shape of the curve looks like a tilted parabola. This can be explained by taking both exciton-exciton interaction and saturation effect into account. Inset shows exciton-exciton interaction monotonically decreases with increasing  $|C|$  (cyan curve); on the other hand, the saturation effect initially rises with increasing  $|C|$  but then it decreases (red curve). It can be easily seen that superimposing these two graphs can explain the tilted parabola shape of  $\Delta E_{LP}^{IE}$  in our data. Note that  $|C|$  is not 0.5 at zero detuning  $k_{\parallel}$  because we do multiple exciton coupled oscillator fit. (c) Cartoon showing the IE polariton dispersion at two different excitation powers where the combined effect of exciton-exciton interaction and saturation effect is present. Here,  $X_1$  and  $X_2$  are the exciton energies at power  $P_1$  and  $P_2$ , respectively. In our system, even though the saturation effect outweighs exciton-exciton interaction, the zero detuning  $k_{\parallel}$  increases with increasing power since the exciton blueshifts. We note that  $\Delta E_{exc-exc}$  and  $\Delta E_{sat}$  have the opposite sign for the upper IE polariton branch but have the same sign for the lower IE polariton branch. This leads to a smaller shift of the upper IE polariton branch compared to the lower IE polariton branch at the zero detuning  $k_{\parallel}$ . (d) Calculated  $\Delta E_{exc-exc}$  and  $\Delta E_{sat}$  at the zero detuning  $k_{\parallel}$  from the experimental data as a function polariton density. This confirms  $\Delta E_{sat} > \Delta E_{exc-exc}$  in our system. Error bars are explained in the description of Fig. 3.

## REFERENCES

- <sup>1</sup>N. Gisin and R. Thew, *Nature photonics* **1**, 165 (2007).
- <sup>2</sup>V. Giovannetti, S. Lloyd, and L. Maccone, *Science* **306**, 1330 (2004).
- <sup>3</sup>D. E. Chang, V. Vuletić, and M. D. Lukin, *Nature Photonics* **8**, 685 (2014).
- <sup>4</sup>M. D. Lukin, M. Fleischhauer, R. Cote, L. M. Duan, D. Jaksch, J. I. Cirac, and P. Zoller, *Phys. Rev. Lett.* **87**, 037901 (2001).
- <sup>5</sup>I. Carusotto and C. Ciuti, *Reviews of Modern Physics* **85**, 299 (2013), arXiv:1205.6500.
- <sup>6</sup>G. Muñoz-Matutano, A. Wood, M. Johnsson, X. Vidal, B. Q. Baragiola, A. Reinhard, A. Lemaître, J. Bloch, A. Amo, G. Nogues, B. Besga, M. Richard, and T. Volz, *Nature Materials* **18**, 213 (2019).
- <sup>7</sup>A. Delteil, T. Fink, A. Schade, S. Höfling, C. Schneider, and A. İmamoğlu, *Nature Materials* **18**, 219 (2019).
- <sup>8</sup>D. G. Suárez-Forero, F. Riminucci, V. Ardizzone, N. Karpowicz, E. Maggolini, G. Macorini, G. Lerario, F. Todisco, M. De Giorgi, L. Dominici, D. Ballarini, G. Gigli, A. S. Lanotte, K. West, K. Baldwin, L. Pfeiffer, and D. Sanvitto, *Phys. Rev. Lett.* **126**, 137401 (2021).
- <sup>9</sup>E. Togan, H.-T. Lim, S. Faelt, W. Wegscheider, and A. Imamoglu, *Phys. Rev. Lett.* **121**, 227402 (2018).
- <sup>10</sup>I. Rosenberg, D. Liran, Y. Mazuz-Harpaz, K. West, L. Pfeiffer, and R. Rapaport, *Science Advances* **4** (2018), 10.1126/sciadv.aat8880, <https://advances.sciencemag.org/content/4/10/eaat8880.full.pdf>.
- <sup>11</sup>K. F. Mak and J. Shan, *Nature Photonics* **10**, 216 (2016).
- <sup>12</sup>L. Zhang, F. Wu, S. Hou, Z. Zhang, Y.-H. Chou, K. Watanabe, T. Taniguchi, S. R. Forrest, and H. Deng, *Nature* **591**, 61 (2021).
- <sup>13</sup>E. M. Alexeev, D. A. Ruiz-Tijerina, M. Danovich, M. J. Hamer, D. J. Terry, P. K. Nayak, S. Ahn, S. Pak, J. Lee, J. I. Sohn, *et al.*, *Nature* **567**, 81 (2019).
- <sup>14</sup>L. Zhang, Z. Zhang, F. Wu, D. Wang, R. Gogna, S. Hou, K. Watanabe, T. Taniguchi, K. Kulkarni, T. Kuo, *et al.*, *Nature communications* **11**, 1 (2020).
- <sup>15</sup>Y. Tang, J. Gu, S. Liu, K. Watanabe, T. Taniguchi, J. Hone, K. F. Mak, and J. Shan, *Nature Nanotechnology* **16**, 52 (2021).

- <sup>16</sup>X. Liu, T. Galfsky, Z. Sun, F. Xia, E. C. Lin, Y. H. Lee, S. Kéna-Cohen, and V. M. Menon, *Nature Photonics* **9**, 30 (2014), arXiv:1406.4826.
- <sup>17</sup>Z. Sun, J. Gu, A. Ghazaryan, Z. Shotan, C. R. Consideine, M. Dollar, B. Chakraborty, X. Liu, P. Ghaemi, S. Kéna-Cohen, and V. M. Menon, *Nature Photonics* **11**, 491 (2017).
- <sup>18</sup>Y.-J. Chen, J. D. Cain, T. K. Stanev, V. P. Dravid, and N. P. Stern, *Nature Photonics* **11**, 431 (2017).
- <sup>19</sup>S. Dufferwiel, T. P. Lyons, D. D. Solnyshkov, A. A. P. Trichet, F. Withers, S. Schwarz, G. Malpuech, J. M. Smith, K. S. Novoselov, M. S. Skolnick, D. N. Krizhanovskii, and A. I. Tartakovskii, *Nature Photonics* **11**, 497 (2017).
- <sup>20</sup>L. B. Tan, O. Cotlet, A. Bergschneider, R. Schmidt, P. Back, Y. Shimazaki, M. Kroner, and A. m. c. İmamoğlu, *Phys. Rev. X* **10**, 021011 (2020).
- <sup>21</sup>R. P. A. Emmanuele, M. Sich, O. Kyriienko, V. Shahnazaryan, F. Withers, A. Catanzaro, P. M. Walker, F. A. Benimetskiy, M. S. Skolnick, A. I. Tartakovskii, I. A. Shelykh, and D. N. Krizhanovskii, *Nature Communications* **11**, 3589 (2020).
- <sup>22</sup>V. Kravtsov, E. Khestanova, F. A. Benimetskiy, T. Ivanova, A. K. Samusev, I. S. Sinev, D. Pidgayko, A. M. Mozharov, I. S. Mukhin, M. S. Lozhkin, *et al.*, *Light: Science & Applications* **9**, 1 (2020).
- <sup>23</sup>J. Gu, V. Walther, L. Waldecker, D. Rhodes, A. Raja, J. C. Hone, T. F. Heinz, S. Kéna-Cohen, T. Pohl, and V. M. Menon, *Nature Communications* **12**, 2269 (2021).
- <sup>24</sup>P. Rivera, J. R. Schaibley, A. M. Jones, J. S. Ross, S. Wu, G. Aivazian, P. Klement, K. Seyler, G. Clark, N. J. Ghimire, *et al.*, *Nature communications* **6**, 1 (2015).
- <sup>25</sup>N. Leisgang, S. Shree, I. Paradisanos, L. Sponfeldner, C. Robert, D. Lagarde, A. Balocchi, K. Watanabe, T. Taniguchi, X. Marie, *et al.*, *Nature Nanotechnology* **15**, 901 (2020).
- <sup>26</sup>E. Lorchat, M. Selig, F. Katsch, K. Yumigeta, S. Tongay, A. Knorr, C. Schneider, and S. Höfling, *Physical Review Letters* **126**, 037401 (2021).
- <sup>27</sup>I. C. Gerber, E. Courtade, S. Shree, C. Robert, T. Taniguchi, K. Watanabe, A. Balocchi, P. Renucci, D. Lagarde, X. Marie, *et al.*, *Physical Review B* **99**, 035443 (2019).
- <sup>28</sup>N. Peimyoo, T. Deilmann, F. Withers, J. Escolar, D. Nutting, T. Taniguchi, K. Watanabe, A. Taghizadeh, M. F. Craciun, K. S. Thygesen, *et al.*, *Nature Nanotechnology* , 1 (2021).
- <sup>29</sup>T. Deilmann and K. S. Thygesen, *Nano letters* **18**, 2984 (2018).
- <sup>30</sup>D. Erckensten, S. Brem, and E. Malic, *Physical Review B* **103**, 045426 (2021).

- <sup>31</sup>M. Glazov, H. Ouerdane, L. Pilozzi, G. Malpuech, A. Kavokin, and A. d'Andrea, *Physical Review B* **80**, 155306 (2009).
- <sup>32</sup>L. Wang, I. Meric, P. Huang, Q. Gao, Y. Gao, H. Tran, T. Taniguchi, K. Watanabe, L. Campos, D. Muller, *et al.*, *Science* **342**, 614 (2013).

# Supplementary Materials: Highly non-linear interlayer exciton-polaritons in bilayer $\text{MoS}_2$

## I. DEVICE FABRICATION

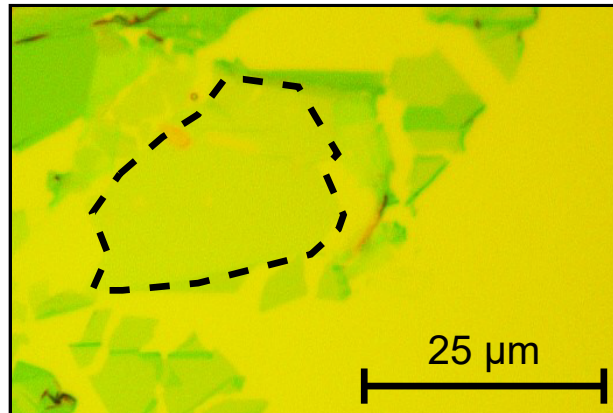


FIG. S1. **Optical micrograph of the device.** (a) Optical micrograph of the hBN/ $\text{MoS}_2$  bilayer/hBN heterostructure on a distributed Bragg reflector (DBR) before top silver mirror deposition. The dashed line marks the uniform area of the heterostructure where measurements are done.

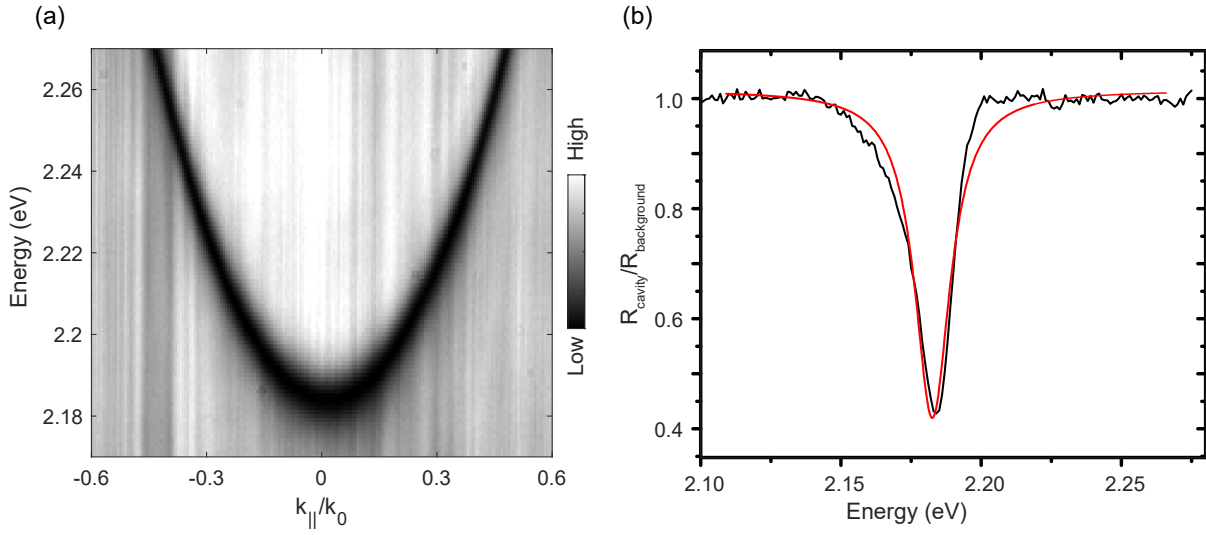


FIG. S2. **PMMA bare cavity mode.** (a) Dispersion of the PMMA bare cavity mode measured away from the hBN/bilayer MoS<sub>2</sub>/hBN heterostructure. The bare cavity mode gets 0.23 eV red shifted on the sample area due to the hBN and bilayer MoS<sub>2</sub>. (b) Line cut of the bare cavity mode at  $k_{||} = 0$ . The red curve is the fitted Lorentzian with a FWHM of 15.5 meV.

## II. DETAILS OF COUPLED OSCILLATOR MODEL

The five polariton branches in our experiment can be described with the eigen modes of the following five coupled oscillator model.

$$\begin{pmatrix} E_{cav} & \Omega_A & \Omega_{IE} & \Omega_{A2s} & \Omega_B \\ \Omega_A & E_A & 0 & 0 & 0 \\ \Omega_{IE} & 0 & E_{IL} & 0 & 0 \\ \Omega_{A2s} & 0 & 0 & E_{A2s} & 0 \\ \Omega_B & 0 & 0 & 0 & E_B \end{pmatrix}$$

where  $E_{cav} = \frac{c\hbar}{\text{enc}} \sqrt{k_v^2 + k_{||}^2} = \frac{c\hbar}{\text{enc}} \sqrt{k_v^2 + \left(10^7 \frac{k_{||}}{k_0}\right)^2}$ ,  $k_v = \frac{2\pi}{\lambda_c} n_c$ ,  $k_0 = \frac{2\pi}{\lambda_c} \approx 10^7 \text{ nm}^{-1}$ ,  $e$  is the electronic charge. Here the wavelength is in meter and energy is in eV. The subscripts cav, A, IE, A2s, and B refer to the cavity mode, A exciton, interlayer exciton, 2s state of A exciton, and B exciton respectively.  $\Omega_X$  and  $E_X$  refer to the Rabi splitting and energy of the X exciton respectively.

The fitting yields  $\lambda_c = 636.38 \text{ nm}$ ,  $n_c = 1.47$ ,  $E_{A1s} = 1.9323 \text{ eV}$ ,  $E_{IL} = 2.0014 \text{ eV}$ ,  $E_{A2s} = 2.0819 \text{ eV}$ ,  $E_{B1s} = 2.0994 \text{ eV}$  and the Rabi splittings  $\Omega_{A1s} = 40.4 \text{ meV}$ ,  $\Omega_{IL} = 21.4 \text{ meV}$ ,  $\Omega_{A2s} = 26 \text{ meV}$ ,  $\Omega_{B1s} = 51 \text{ meV}$ .

### III. STRONG COUPLING OF THE IE AND A EXCITON AT 77 K

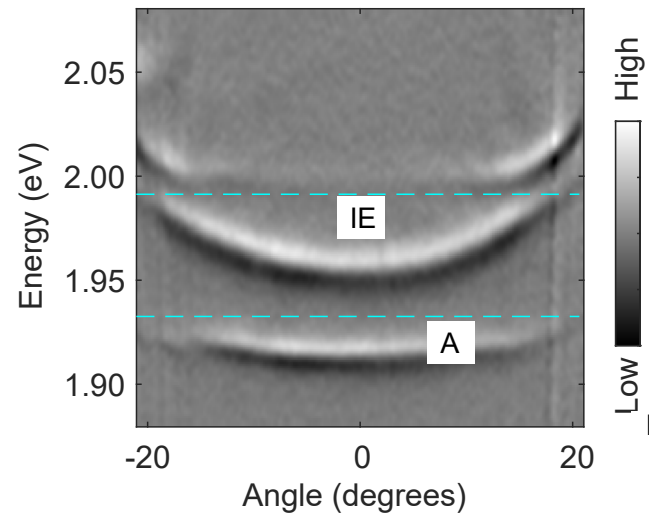


FIG. S3. Strong coupling of the IE and A exciton at 77 K in bilayer MoS<sub>2</sub>.

#### IV. DETAILS OF THE POLARITON DENSITY CALCULATION

Polariton density is calculated from the Gross-Pitaevskii (GP) equation. The GP equation at wavevector  $k$  can be written as

$$i\hbar \frac{\partial \psi_{LP}(k, t)}{\partial t} = \left[ \epsilon_{LP}(k) - \frac{i\hbar\gamma_{LP}}{2} \right] \psi_{LP}(k, t) + \hbar F_P(k, t) \quad (\text{S1})$$

Here  $\epsilon_{LP}(k) = \hbar\omega_{LP}(k)$  is the energy of the lower polariton of an exciton and  $\gamma_{LP}$  is the line width of the polariton.  $F_P(k, t)$  is the coherent driving. The pulse width of our supercontinuum laser is 20 ps which is much larger than the polariton lifetime (30-50 fs). This allows the pumping to be treated as continuous wave which is resonant with our cavity. We can express the pumping term as  $F_P(k, t) = F_P(k)e^{-i\omega_P t}$  and  $\psi_{LP}(k, t) = \tilde{\psi}_{LP}(k)e^{-i\omega_P t}$  where  $\omega_P$  is the pump frequency. This simplifies the above equation to

$$\left[ \hbar\omega_P - \epsilon_{LP}(k) + \frac{i\hbar\gamma_{LP}}{2} \right] \tilde{\psi}_{LP}(k) = \hbar F_P(k) \quad (\text{S2})$$

The  $F_P(k)$  term can be written from the input-output relation.

$$F_P(k) = C(k) \sqrt{\frac{\eta \cdot P_{\text{int}}(k)}{\hbar\omega_P}} \quad (\text{S3})$$

$$\eta = \frac{|t_{\text{top mirror}}|^2}{\tau_{\text{trip}}} \quad (\text{S4})$$

Here  $C(k)$  is the photon Hopfield coefficient of the polariton branch.  $P_{\text{int}}(k)$  is the incident power on the top mirror and  $\eta$  is the coupling coefficient.  $t_{\text{top mirror}}$  is the transmission of top mirror, and  $\tau_{\text{trip}}$  is the photon trip time in the cavity. This gives  $\eta = 4.1 \times 10^{12} \text{ s}^{-1}$ . Equation S2 can be written as

$$\tilde{\psi}_{LP}(k, \omega_P) = \frac{\hbar F_P(k)}{\hbar\omega_P - \epsilon_{LP}(k) + \frac{i\hbar\gamma_{LP}}{2}} \quad (\text{S5})$$

Polariton density at the wavevector  $k$  and frequency  $\omega_P$  is

$$|\psi_{LP}(k, \omega_P, t)|^2 = \left| \tilde{\psi}_{LP}(k, \omega_P) \right|^2 = \frac{|C|^2 \frac{\eta \cdot P_{\text{int}}(k)}{\hbar\omega_P}}{(\omega_P - \omega_{LP}(k))^2 + \left(\frac{\gamma_{LP}}{2}\right)^2} \quad (\text{S6})$$

Since the polaritons have a finite width in energy, the total polariton density at the wavevector  $k$  can be found out by integrating over the all frequency range

$$\left| \tilde{\psi}_{LP}(k) \right|^2 = \int \frac{|C|^2 \eta \cdot \xi(k, \omega_P)}{(\omega_P - \omega_{LP}(k))^2 + \left(\frac{\gamma_{LP}}{2}\right)^2} d\omega_P \quad (S7)$$

Here,  $\xi(k, \omega_P)$  denotes the incident power density (power/frequency/wavevector).

The integral above can be numerically calculated but we can make an approximation to get a close form solution for the density. We note that the Lorentzian part of the integrand for  $\gamma_{LP} \rightarrow 0$  is a Dirac delta function

$$\delta(\omega_P - \omega_{LP}) = \lim_{\gamma_{LP} \rightarrow 0} \frac{1}{\pi} \frac{\frac{\gamma_{LP}}{2}}{(\omega_P - \omega_{LP})^2 + \left(\frac{\gamma_{LP}}{2}\right)^2} \quad (S8)$$

Using the above formula and taking the power density  $\xi(k, \omega_P)$  constant over the narrow range of excitation we get

$$\left| \tilde{\psi}_{LP}(k) \right|^2 \approx \frac{2\pi |C|^2 \eta \cdot \xi}{\hbar \omega_{LP}(k) \gamma_{LP}(k)} \quad (S9)$$

Here,  $\gamma_{LP}(k)$  is determined from the experimental data.

Total real space polariton density can be found out by summing  $\left| \tilde{\psi}_{LP}(k) \right|^2$  in the  $k$ -space for the experimental wavevector range

$$\left| \tilde{\psi}_{LP} \right|^2 = \sum_{k=k_{min}}^{k_{max}} \left| \tilde{\psi}_{LP}(k) \right|^2 = \frac{2\pi |C|^2 \eta \cdot \xi}{\hbar} \sum_{k=k_{min}}^{k_{max}} \frac{1}{\omega_{LP}(k) \gamma_{LP}(k)} \quad (S10)$$

If  $P_0$  is the measured real space peak power density (power/energy) of the pulsed super-continuum laser excitation then  $\xi = P_0/N$ , where  $N$  is the number of  $k$  point in between  $k_{min}$  and  $k_{max}$ .

## V. RAW DATA FOR THE NONLINEARITY OF THE IE POLARITON

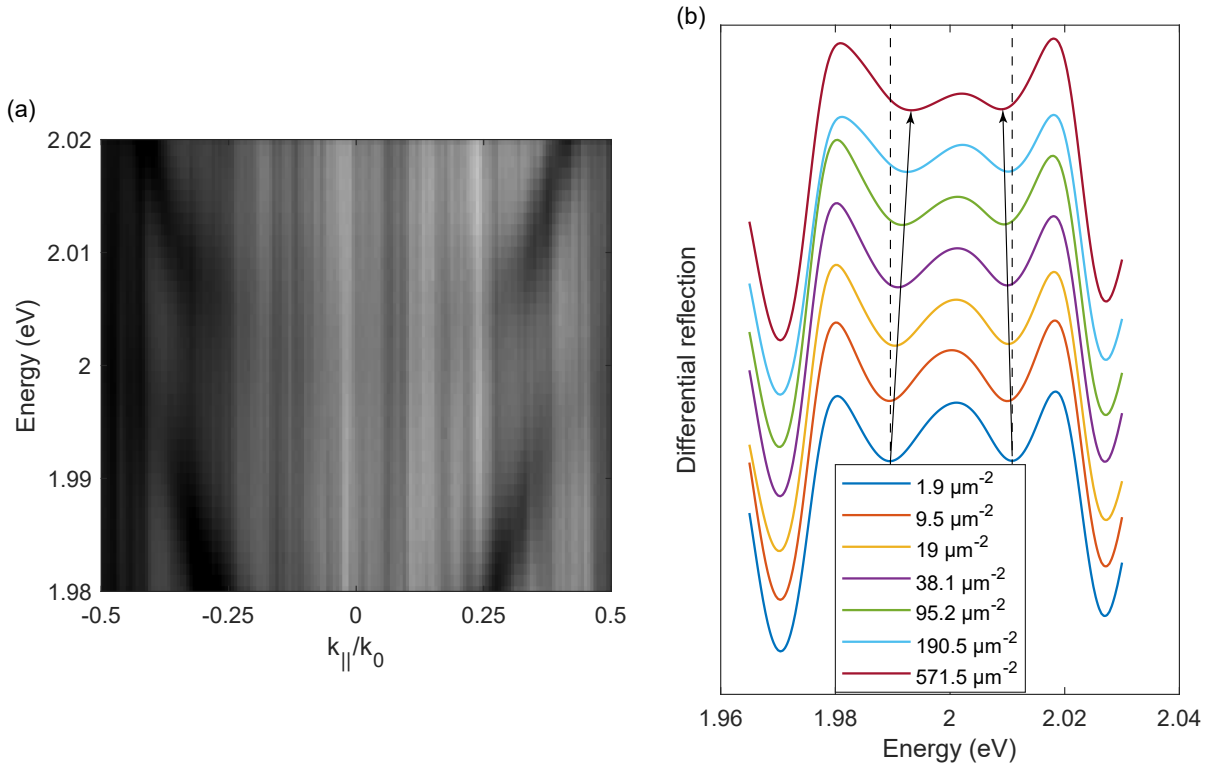


FIG. S4. **Raw data for the nonlinearity of the IE polariton at 7 K.** (a) K-space differential reflection data showing the dispersion of the IE lower branch (pol-2) and IE upper branch (pol-3) at the lowest density ( $1.9 \mu\text{m}^{-2}$ ). The excitation bandwidth of the supercontinuum laser for the IE is set 40 meV by using a low-pass and a high-pass filter. (b) Line cut of the k-space data at zero detuning  $k_{\parallel}$  showing the differential reflection of the IE lower branch (pol-2) and IE upper branch (pol-3) at different polariton density. Note that since the IE exciton blueshifts with increasing density, the zero detuning  $k_{\parallel}$  also increases with increasing density.

Fig. S4b shows the differential reflection at the zero detuning  $k_{\parallel}$  for IL exciton polariton. The upper polariton branch red shifts and lower polariton branch blue shifts with increasing density reducing the Rabi splitting. We also notice that the two branches move asymmetrically – the lower branch moves more than the upper branch at zero detuning  $k_{\parallel}$ . This is because both exciton-exciton interaction and saturation give rise to blue shift for the lower branch but they produce opposite shift for the upper branch – as described in the main text.

## VI. SATURATION NONLINEARITY OF THE EXCITONS MEASURED IN OPEN CAVITY GEOMETRY

To examine the nonlinearity of the bare excitons even before they form polariton in a cavity, we studied power dependence on the same bilayer MoS<sub>2</sub> sample before depositing the top mirror. We observe that the amplitude of the differential reflection dip for both A and interlayer exciton reduces with increasing power; the FWHM of the lineshape also increases for both A and interlayer exciton with increasing power, see Fig. 4a and Fig. 4b. We analyze the area under the differential reflection curve as a function of excitation power. The area under the curve can be mapped to the oscillator strength assuming that the area under the differential reflection curve is proportional to the oscillator strength, see Fig. 4c and Fig. 4d. Here,  $f_X$  and  $f_{X0}$  denote the oscillator strength of the exciton X at a given power value and at the starting power value respectively. We can see that the interlayer exciton absorption starts saturating at much lower power values than the A exciton. Comparing the power axis of Fig. 4c and Fig. 4d, we notice that the interlayer exciton reaches the same level of saturation at almost an order of magnitude lower power value than A exciton. The enhancement of the saturation of the interlayer exciton in open cavity measurements is similar to the 10 fold enhancement of the nonlinearity for interlayer polariton. The solid lines in Fig. 4c and Fig. 4d are the power-law fits of the data. Empirically, we can fit the decay of the oscillator strength with excitation power (P) for the IE and A exciton with power-law  $P^{-0.43}$  and  $P^{-0.25}$  respectively. This shows that not only does the interlayer exciton saturates at lower power but the decay of the oscillator strength for IE is faster as well compared to that of the A exciton.

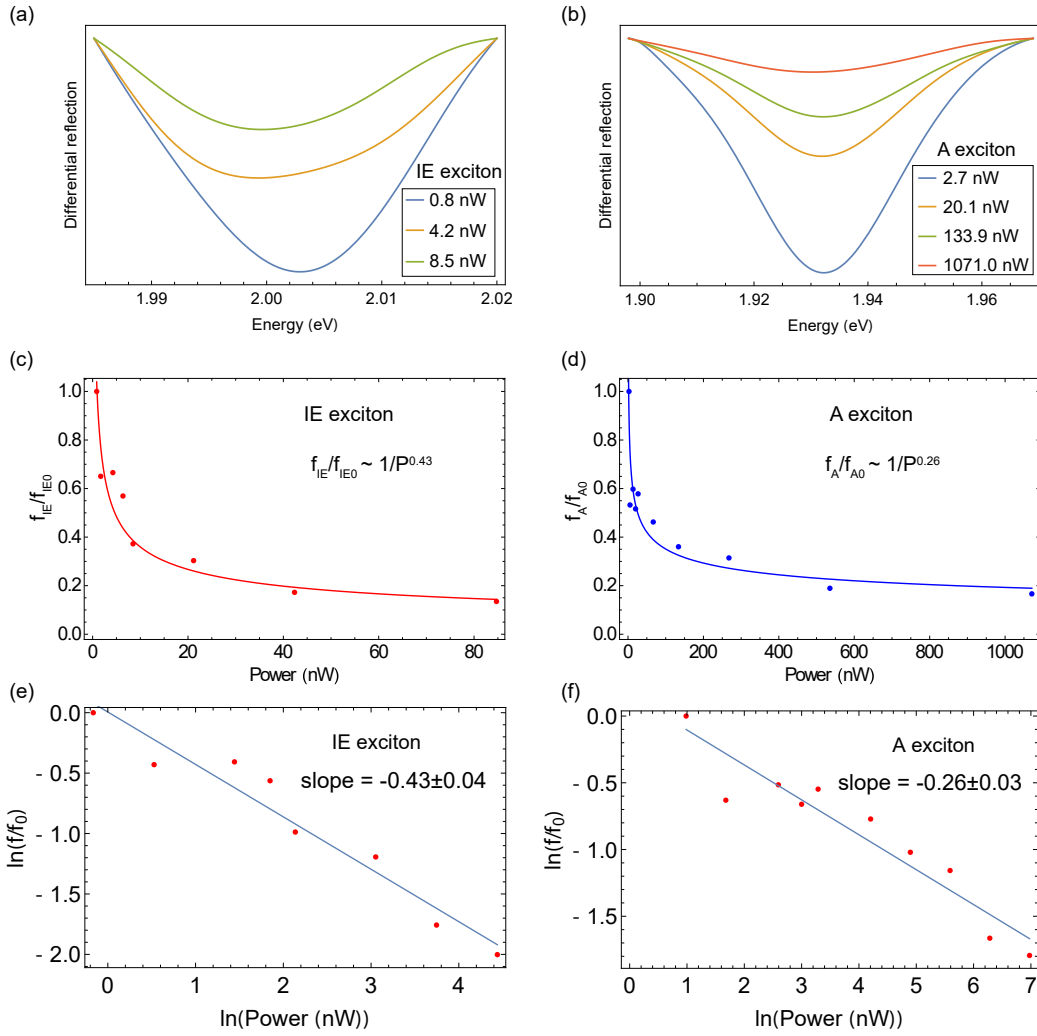


FIG. S5. **Saturation of the excitons with excitation power measured in open cavity (before spinning the PMMA and evaporation of the silver mirror) at 77 K.** (a) and (b) show the differential reflection of the IE and A excitons as a function of incident power. A linear baseline is subtracted from the data. The excitation bandwidth for IE and A exciton are kept 36 meV and 71 meV respectively around their exciton energies. (c) and (d) show the decrease of the oscillator strength with increasing power for IE and A exciton respectively.  $f_X$  and  $f_{X0}$  denote the oscillator strength of X exciton at a given power and at the lowest power respectively. Oscillator strength of the excitons are assumed proportional to the area under the differential reflection curve. The superimposed lines are the polynomial fit. This shows that not only does the interlayer exciton saturates at lower power but the power law decay of the oscillator strength for IE is faster as well compared to that of the A exciton. (e) and (f) show the same power law fit shown in panel (c) and (d) in logarithmic scale.

## VII. HOPFIELD COEFFICIENTS OF A EXCITON

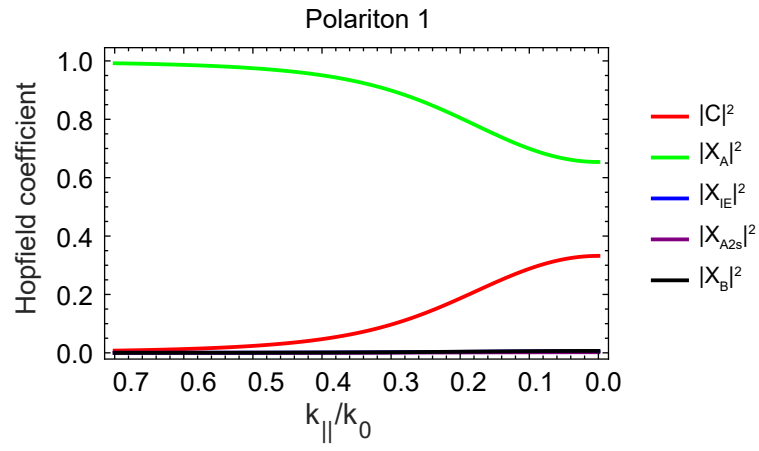


FIG. S6. Hopfield coefficients of A exciton.

## VIII. RABI SPLITTING OF INTERLAYER EXCITON POLARITON AS A FUNCTION OF POLARITON DENSITY

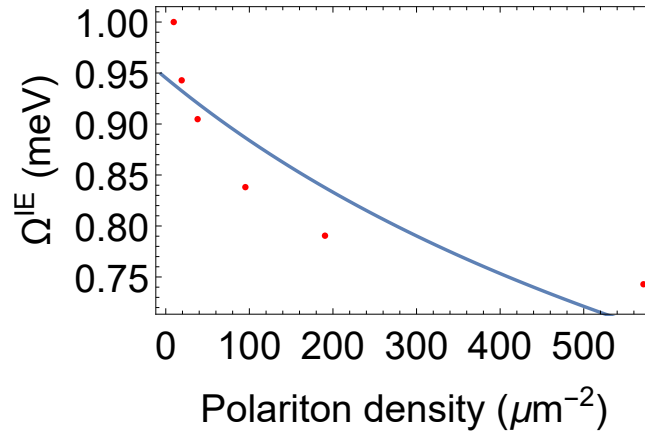


FIG. S7. Rabi splitting of IE polariton at the zero detuning  $k_{\parallel}$  as a function of polariton density at 7 K. The blue line is the fit to the usual formula  $\Omega = \frac{\Omega_0}{\sqrt{1 + \frac{n}{n_{\text{sat}}}}}$  for free 2D excitons.

We plot the Rabi splitting of the IE polariton at the zero detuning  $k_{\parallel}$  as a function of density, see Fig. S7. We note that the usual formula for free 2D excitons  $\Omega = \frac{\Omega_0}{\sqrt{1 + \frac{n}{n_{\text{sat}}}}}$  does not fit our data well. The inadequacy of the free 2D exciton formula to describe the density dependence of the Rabi splitting was also observed in a recent study<sup>S12</sup> on the Moiré exciton-polariton in a hetrobilayer TMDC.

## IX. ENERGY OF THE LOWER BRANCH OF A EXCITON POLARITON AS A FUNCTION OF POLARITON DENSITY

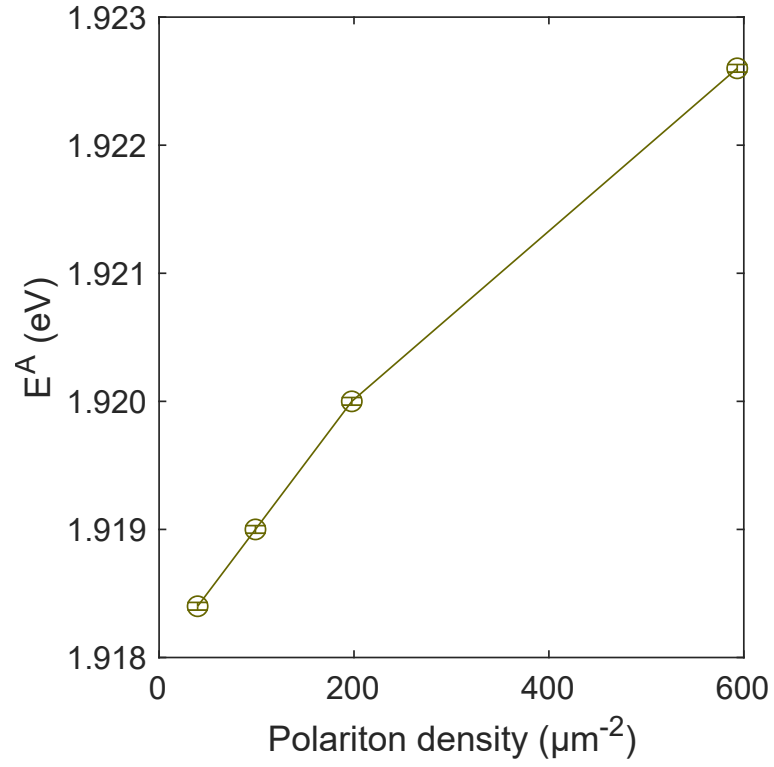


FIG. S8. Energy of the lower branch of A exciton polariton as a function of polariton density at 7 K from which the  $g_{LP}^A$  is calculated and plotted in Fig.3b of the main manuscript.